

On a Helmholtz transmission problem in planar domains with corners

Johan Helsing^{a,*}, Anders Karlsson^b

^aCentre for Mathematical Sciences, Lund University, Box 118, 221 00 Lund, Sweden

^bElectrical and Information Technology, Lund University, Box 118, 221 00 Lund, Sweden

Abstract

A particular mix of integral equations and discretization techniques is suggested for the solution of a planar Helmholtz transmission problem with relevance to the study of surface plasmon waves. The transmission problem describes the scattering of a time-harmonic transverse magnetic wave from an infinite dielectric cylinder with complex permittivity and sharp edges. Numerical examples illustrate that the resulting scheme is capable of obtaining total magnetic and electric fields to very high accuracy in the entire computational domain.

Keywords: Corner singularity, Helmholtz equation, Nyström discretization, Scattering, Surface plasmon wave

2010 MSC: 78M15, 65N38, 35Q60, 35J05, 31A10

1. Introduction

This paper is about solving a classic transmission problem for the Helmholtz equation in the plane using integral equation techniques. A physical interpretation is that an incident time-harmonic transverse magnetic wave, in a medium with unit permittivity, is scattered from a homogeneous dielectric cylindrical object with permittivity ε . The problem is to find the total magnetic field U everywhere.

When ε is real and positive and when the object boundary Γ is smooth, this problem is uncomplicated. Efficient boundary integral equations and fast solution techniques have long since been established and their use in computational physics is standard practice. See [26] for pioneering numerical work and [7] for an overview of more recent development. The only issue that, perhaps, still is not completely resolved is how to compute U and its gradient ∇U in an appropriate fashion close to Γ in a post-processor [1, 21].

*Corresponding author. URL: <http://www.maths.lth.se/na/staff/helsing/>

Email addresses: helsing@maths.lth.se (Johan Helsing),
anders.karlsson@eit.lth.se (Anders Karlsson)

When ε is not real and positive and when Γ is not smooth, the transmission problem gets harder. Issues arise relating to modeling, the existence and the uniqueness of solutions, and resolution. A particularly difficult situation is when ε is real and negative and Γ has sharp corners. The excitation of rapidly oscillating corner fields and their interaction with surface plasmon waves then make the choice of integral equations and discretization techniques crucial. To our knowledge, integral equation methods have not been used in this context, but a finite element solver has recently been developed [5]. This solver, which relies on so-called perfectly matched layers at the corners, is capable of producing convergent results also for challenging setups.

We will review integral equations for the Helmholtz transmission problem and show that a system of equations due to Kleinman and Martin [20] is well suited for our purposes. In passing we observe that another, seldom used, integral equation from [20] is surprisingly efficient when ε is real and positive and when the accurate evaluation of ∇U close to Γ is of concern. The successful use of integral equations in computations is, of course, coupled to the choice of discretization scheme. We use standard Nyström discretization, accelerated with recursively compressed inverse preconditioning, and product integration for the evaluation of layer potentials close to their sources [9, 11]. As a result, we can solve the transmission problem for negative ε (in a limit sense) in domains with corners and rapidly obtain corner fields and surface plasmon waves with a precision of about thirteen digits, even close to Γ .

The rest of the paper is organized as follows: Section 2 presents the transmission problem as a system of partial differential equations (PDEs). Section 3 reviews some popular integral equation reformulations which all work well for ε real and positive. This includes three systems of integral equations which we call KM0, KM1, and KM2. Section 4 is on discretization. Special emphasis is given to the treatment of singularities and near-singularities of kernels that occur in field representations and systems of integral equations. The basic evaluation strategy is the same as in [9, 12], but the treatment of the hypersingularity in the gradient of the acoustic double layer potential operator is new. Section 5 reviews results on the existence and uniqueness of solutions to the PDEs and to the integral equations of KM0, KM1, and KM2. These issues are extremely important when ε is not real and positive and Γ has sharp corners. For inadmissible ε , there simply is no solution. For a discrete set of other ε , an inappropriate choice of integral equations may lead to numerical failure. In Sections 6, 7, and 8 we strive to summarize the fascinating physics which is illustrated by the numerical examples at the end of the paper.

2. PDE formulation of the transmission problem

A homogeneous dielectric object, a domain Ω_2 with boundary Γ , is embedded in a homogeneous dielectric medium Ω_1 in the plane \mathbb{R}^2 . The outward unit normal at position $r = (x, y)$ on Γ is ν . The ratio between the permittivities in Ω_2 and Ω_1 is ε . An incident plane wave

$$U^{\text{in}}(r) = e^{ik_1(r \cdot d)}, \quad r \in \mathbb{R}^2, \quad (1)$$

has wavenumber k_1 , where $\Re\{k_1\} \geq 0$, and direction d . Let the wavenumber in Ω_2 be

$$k_2 = \sqrt{\varepsilon}k_1. \quad (2)$$

A transmission problem for the Helmholtz equation can now be formulated: find $U(r)$ which solves the system of PDEs

$$\Delta U(r) + k_1^2 U(r) = 0, \quad r \in \Omega_1, \quad (3)$$

$$\Delta U(r) + k_2^2 U(r) = 0, \quad r \in \Omega_2, \quad (4)$$

with boundary conditions

$$\lim_{\Omega_1 \ni r \rightarrow r^\circ} U(r) = \lim_{\Omega_2 \ni r \rightarrow r^\circ} U(r), \quad r^\circ \in \Gamma, \quad (5)$$

$$\lim_{\Omega_1 \ni r \rightarrow r^\circ} \varepsilon \nu^\circ \cdot \nabla U(r) = \lim_{\Omega_2 \ni r \rightarrow r^\circ} \nu^\circ \cdot \nabla U(r), \quad r^\circ \in \Gamma, \quad (6)$$

$$U(r) = U^{\text{in}}(r) + U^{\text{sc}}(r), \quad r \in \Omega_1, \quad (7)$$

$$U^{\text{sc}}(r) = \frac{e^{ik|r|}}{\sqrt{|r|}} \left(F(r/|r|) + \mathcal{O}\left(\frac{1}{|r|}\right) \right), \quad |r| \rightarrow \infty. \quad (8)$$

Here $U^{\text{sc}}(r)$ is the scattered field, $F(r/|r|)$ is the far-field pattern, and (8) is the two-dimensional analogue of the radiation condition [4, Eq. (6.22b)].

We are chiefly interested in computing the real fields

$$H(r, t) = \Re \{ U(r) e^{-it} \}, \quad r \in \Omega_1 \cup \Omega_2, \quad (9)$$

$$\nabla H(r, t) = \Re \{ \nabla U(r) e^{-it} \}, \quad r \in \Omega_1 \cup \Omega_2, \quad (10)$$

where t denotes time and angular frequency is scaled to one. The field $H(r, t)$ can be interpreted as a time-harmonic magnetic wave in a setting where the PDE models a three-dimensional transverse translation-invariant electromagnetic transmission problem for the Maxwell equations, with magnetic and electric fields

$$\mathbf{H}(r) = U(r) \hat{\mathbf{z}}, \quad (11)$$

$$\mathbf{E}(r) = \begin{cases} ik_1^{-1} \nabla U(r) \times \hat{\mathbf{z}}, & r \in \Omega_1, \\ ik_1^{-1} \varepsilon^{-1} \nabla U(r) \times \hat{\mathbf{z}}, & r \in \Omega_2. \end{cases} \quad (12)$$

Here $\hat{\mathbf{z}}$ is a unit vector perpendicular to the plane, the electric field is scaled with the wave impedance of free space, and the gradient $\nabla U(r)$ is augmented with a zero third component in the cross product.

3. Integral equation formulations

This section reviews some popular integral equation reformulations of the transmission problem in Section 2 in a uniform notation.

3.1. Bessel functions, kernels, and vectors

In what follows, $J_n(x)$ and $Y_n(x)$ are n th order Bessel function of the first and second kind and

$$H_n^{(1)}(x) = J_n(x) + iY_n(x) \quad (13)$$

is the n th order Hankel function of the first kind. We extend the definition of the outward unit normal $\nu = \nu(r)$ at a point $r \in \Gamma$ so that if $r \notin \Gamma$, then ν is to be interpreted as an arbitrary unit vector associated with r . The fundamental solution to the Helmholtz equation is taken to be

$$\Phi_k(r, r') = \frac{i}{2} H_0^{(1)}(k|r - r'|), \quad (14)$$

where k is a wavenumber. We shall also use the double-layer type kernels with $r' \in \Gamma$ and $\nu' = \nu(r')$ the outward unit normal at r' ,

$$D(r, r') = -\frac{\nu \cdot (r - r')}{|r - r'|^2} \quad \text{and} \quad D(r', r) = \frac{\nu' \cdot (r - r')}{|r - r'|^2}. \quad (15)$$

The boundary Γ has positive orientation and a parameterization called $r(s)$.

At times we identify vectors r, r', ν, ν' in the real plane \mathbb{R}^2 with points z, τ, n_z, n_τ in the complex plane \mathbb{C} . Conjugation of complex quantities is indicated with an overbar symbol.

3.2. A standard choice of operators

We use standard definitions of the single- and double-layer potentials and their normal derivatives [4, Eqs. (3.8)–(3.11)]

$$S_k \rho(r) = \int_{\Gamma} \Phi_k(r, r') \rho(r') \, d\ell', \quad (16)$$

$$K_k \rho(r) = \int_{\Gamma} \frac{\partial \Phi_k}{\partial \nu'}(r, r') \rho(r') \, d\ell', \quad (17)$$

$$K_k^A \rho(r) = \int_{\Gamma} \frac{\partial \Phi_k}{\partial \nu}(r, r') \rho(r') \, d\ell', \quad (18)$$

$$T_k \rho(r) = \int_{\Gamma} \frac{\partial^2 \Phi_k}{\partial \nu \partial \nu'}(r, r') \rho(r') \, d\ell', \quad (19)$$

where $d\ell$ is an element of arc length, $\partial/\partial \nu = \nu(r) \cdot \nabla$, and $\partial/\partial \nu' = \nu(r') \cdot \nabla'$. Note that [4] uses a prefactor $i/4$ in the expression corresponding to (14) and a prefactor 2 in the integrals corresponding to (16)–(19). This does not

affect the definitions of S_k , K_k , K_k^A , and T_k : they are the same in (16)–(19) as in [4, Eqs. (3.8)–(3.11)].

For $r \in \Gamma$ it holds [4, Eqs. (3.12)–(3.13)]

$$K_k K_k - S_k T_k = I, \quad (20)$$

$$K_k^A K_k^A - T_k S_k = I. \quad (21)$$

3.3. The first set of Kleinman–Martin equations

Kleinman and Martin [20, Section 4.1] suggest the field representation

$$U(r) = U^{\text{in}}(r) + \frac{1}{2} K_{k_1} \mu(r) + \frac{1}{2} S_{k_1} \rho(r), \quad r \in \Omega_1, \quad (22)$$

$$U(r) = \frac{\varepsilon}{2} K_{k_2} \mu(r) + \frac{c}{2} S_{k_2} \rho(r), \quad r \in \Omega_2, \quad (23)$$

where c is a constant such that $c + \varepsilon \neq 0$ and

$$\arg(c) = \begin{cases} \arg(\varepsilon k_2) & \text{if } \Re\{k_1\} \geq 0, \\ \arg(\varepsilon k_2) - \pi & \text{if } \Re\{k_1\} < 0. \end{cases} \quad (24)$$

The corresponding system of integral equations is

$$\begin{bmatrix} I - \alpha_2 K_{k_2} + \alpha_1 K_{k_1} & -\alpha_1 (c S_{k_2} - S_{k_1}) \\ \alpha_4 (T_{k_2} - T_{k_1}) & I + c \alpha_3 K_{k_2}^A - \alpha_4 K_{k_1}^A \end{bmatrix} \begin{bmatrix} \mu(r) \\ \rho(r) \end{bmatrix} = \begin{bmatrix} f_1(r) \\ f_2(r) \end{bmatrix}, \quad (25)$$

with $r \in \Gamma$ and

$$f_1(r) = -2\alpha_1 U^{\text{in}}(r), \quad f_2(r) = 2\alpha_4 \frac{\partial U^{\text{in}}}{\partial \nu}(r), \quad (26)$$

$$\alpha_1 = \frac{1}{1 + \varepsilon}, \quad \alpha_2 = \frac{\varepsilon}{1 + \varepsilon}, \quad \alpha_3 = \frac{1}{c + \varepsilon}, \quad \alpha_4 = \frac{\varepsilon}{c + \varepsilon}. \quad (27)$$

The choice c in (24) guarantees the uniqueness of the solution μ , ρ to (25) under certain conditions. See, further, Section 5.2.

The equations (22), (23), and (25) will be referred to as the KM1 representation and system, or simply the KM1 equations.

3.4. The second set of Kleinman–Martin equations

Kleinman and Martin [20, Section 4.2] also suggest the field representation

$$U(r) = U^{\text{in}}(r) + \frac{1}{2} K_{k_1} \mu(r) - \frac{1}{2} S_{k_1} \rho(r), \quad r \in \Omega_1, \quad (28)$$

$$U(r) = -\frac{1}{2} K_{k_2} \mu(r) + \frac{\varepsilon}{2} S_{k_2} \rho(r), \quad r \in \Omega_2, \quad (29)$$

where the layer densities μ and ρ have the physical interpretations

$$\mu(r) = \lim_{\Omega_1 \cup \Omega_2 \ni r \rightarrow r^\circ} U(r), \quad r^\circ \in \Gamma, \quad (30)$$

$$\rho(r) = \lim_{\Omega_1 \ni r \rightarrow r^\circ} \nu^\circ \cdot \nabla U(r), \quad r^\circ \in \Gamma. \quad (31)$$

Taking the limit $r \rightarrow \Gamma$ in (28) and (29) gives two integral equations. The limits of the gradients in (28) and (29) give two additional equations. In [20, Section 4.2], these four equations are combined into the system of integral equations

$$\begin{bmatrix} I + \alpha_1 K_{k_2} - \alpha_2 K_{k_1} & -\alpha_2 (S_{k_2} - S_{k_1}) \\ \alpha_1 (T_{k_2} - T_{k_1}) & I - \alpha_2 K_{k_2}^\Lambda + \alpha_1 K_{k_1}^\Lambda \end{bmatrix} \begin{bmatrix} \mu(r) \\ \rho(r) \end{bmatrix} = \begin{bmatrix} f_1(r) \\ f_2(r) \end{bmatrix}, \quad (32)$$

with $r \in \Gamma$ and

$$f_1(r) = 2\alpha_2 U^{\text{in}}(r), \quad f_2(r) = 2\alpha_1 \frac{\partial U^{\text{in}}}{\partial \nu}(r), \quad (33)$$

$$\alpha_1 = \frac{1}{1 + \varepsilon}, \quad \alpha_2 = \frac{\varepsilon}{1 + \varepsilon}. \quad (34)$$

The equations (28), (29), and (32) will be referred to as the KM2 representation and system, or simply the KM2 equations.

An advantage with the KM2 representation is that, by adding the null fields of [20, Eqs. (3.15a) and (3.14b)]

$$0 = -\frac{1}{2} K_{k_2} \mu(r) + \frac{\varepsilon}{2} S_{k_2} \rho(r), \quad r \in \Omega_1, \quad (35)$$

$$0 = U^{\text{in}}(r) + \frac{1}{2} K_{k_1} \mu(r) - \frac{1}{2} S_{k_1} \rho(r), \quad r \in \Omega_2, \quad (36)$$

to (28) and (29), the representation of $U(r)$ can be written

$$U(r) = U^{\text{in}}(r) - \frac{1}{2} (K_{k_2} - K_{k_1}) \mu(r) + \frac{1}{2} (\varepsilon S_{k_2} - S_{k_1}) \rho(r), \quad r \in \Omega_1 \cup \Omega_2. \quad (37)$$

The representation (37) contains the difference operator $K_{k_2} - K_{k_1}$ whose kernel is smoother close to Γ than those of the individual operators K_{k_2} and K_{k_1} in (22), (23), (28), and (29). As we shall see in Section 9.6, the stabilizing effect of using (37) is particularly pronounced when the gradient field $\nabla U(r)$ is computed.

3.5. The equations used by Greengard and Lee

Greengard and Lee use the field representation [7, Eq. (8)] that results from setting $c = 1$ in the KM1 equations. The corresponding system of integral equations [7, Eq. (11)] is therefore identical to (25) with $c = 1$. The equations (22), (23), and (25) with $c = 1$ will be referred to as the KM0 representation and system, or simply the KM0 equations.

3.6. The Kress–Roach and Müller–Rokhlin equations

Kress and Roach [22] and Rokhlin [26] study the transmission problem of Section 2 with the boundary conditions (5) and (6) replaced by

$$\lim_{\Omega_1 \ni r \rightarrow r^\circ} U(r) = \lim_{\Omega_2 \ni r \rightarrow r^\circ} \varepsilon U(r), \quad r^\circ \in \Gamma, \quad (38)$$

$$\lim_{\Omega_1 \ni r \rightarrow r^\circ} \nu^\circ \cdot \nabla U(r) = \lim_{\Omega_2 \ni r \rightarrow r^\circ} \nu^\circ \cdot \nabla U(r), \quad r^\circ \in \Gamma. \quad (39)$$

The field representation and system in [22] is similar to the KM1 equations, but contains two free parameters c_1 and c_2 . One can view the KM1 equations as a simplification of the Kress–Roach equations and we will not investigate the latter equations numerically in this work.

The field representation for $U(r)$ in [26] is

$$U(r) = U^{\text{in}}(r) + \frac{1}{2}K_{k_1}\mu(r) + \frac{1}{2}S_{k_1}\rho(r), \quad r \in \Omega_1, \quad (40)$$

$$U(r) = \frac{1}{2}K_{k_2}\mu(r) + \frac{1}{2\varepsilon}S_{k_2}\rho(r), \quad r \in \Omega_2. \quad (41)$$

This representation gives rise to a system of integral equations, often called the Müller–Rokhlin equations, which is identical to the KM1 system with $c = 1$ and the KM0 system. Since the representation for $U(r)$ in (41) differs from $U(r)$ in (23) with $c = 1$, the expression (9) for $H(r, t)$ changes into

$$H(r, t) = \begin{cases} \Re \{ U(r)e^{-it} \}, & r \in \Omega_1, \\ \Re \{ \varepsilon U(r)e^{-it} \}, & r \in \Omega_2, \end{cases} \quad (42)$$

and the expression (10) for $\nabla H(r, t)$ undergoes an analogous change.

4. Discretization

We discretize and solve the integral equations of Section 3 using Nyström discretization with composite n_{pt} -point Gauss–Legendre quadrature as underlying quadrature. Most often we choose $n_{\text{pt}} = 16$.

When the boundary Γ contains corners, the Nyström scheme is accelerated and stabilized with recursively compressed inverse preconditioning (RCIP). The RCIP technique accomplishes, in linear or sublinear time, a lossless compression of Fredholm second kind integral equations discretized on meshes increasingly *refined* in the direction toward corner vertices. The final preconditioned system is solved for transformed layer densities, represented by their values at discretization points only on a *coarse* mesh on Γ . See the compendium [11] for a thorough review of RCIP acceleration of Nyström schemes. See [13, 15] for applications of these techniques to the solution of integral equations that are similar to those of Section 3. See [10, Section 6.2-6.3] for details on performance enhancement involving Newton’s method and homotopy, and for a discussion of the correspondence between

traditional mesh refinement and the number of recursion steps used in advanced implementations of RCIP. See [16, Section 7.2.2] for general comments on how the need for local resolution, n_{pt} , depends on ε .

When operator kernels $G(r, r')$ contain singularities, or near-singularities, we replace the Gauss–Legendre quadrature, on quadrature panels affected, with a product integration scheme. This scheme was first described in [9, Section 2] and further developed in [12, Section 6] and has as its key the construction of a split

$$G(r, r') d\ell' = G_0(r, r') d\ell' + \log|r - r'|G_L(r, r') d\ell' + \Re \left\{ \frac{G_C(z, \tau) d\tau}{i(\tau - z)} \right\} + \Re \left\{ \frac{G_H(z, \tau) d\tau}{i(\tau - z)^2} \right\}, \quad (43)$$

where $G_0(r, r')$, $G_L(r, r')$, $G_C(z, \tau)$, and $G_H(z, \tau)$ are smooth functions and complex notation is used as explained in Section 3.1. Product integration weights for the kernels of (43) are then obtained using analytical methods and recursion or, when $r \in \Gamma$, alternatively by local regularization [9, Section 2]. The scheme requires explicit formulas for $G(r, r')$, $G_L(r, r')$, $G_C(z, \tau)$, and $G_H(z, \tau)$, while $G_0(r, r')$ needs only to be known if $r \in \Gamma$ and then only in the limit $r' \rightarrow r$.

In the remainder of this section the singular nature of the kernels of S_k , K_k , K_k^A , and T_k is explored, so that splits of the form (43) can be constructed.

4.1. Expansions of $Y_n(x)$ around $x = 0$

The following series expansions [17] of $Y_n(x)$ around $x = 0$ are useful:

$$Y_0(x) = \frac{2}{\pi} J_0(x) \log\left(\frac{x}{2}\right) - \frac{2\psi(1)}{\pi} - \frac{1}{\pi} \sum_{j=1}^{\infty} \frac{(-1)^j 2\psi(j+1)}{j!j!} \left(\frac{x}{2}\right)^{2j}, \quad (44)$$

$$Y_1(x) = \frac{2}{\pi} J_1(x) \log\left(\frac{x}{2}\right) - \frac{2}{\pi x} - \frac{1}{\pi} \sum_{j=0}^{\infty} \frac{(-1)^j (\psi(j+1) + \psi(j+2))}{j!(j+1)!} \left(\frac{x}{2}\right)^{2j+1}, \quad (45)$$

$$Y_2(x) = \frac{2}{\pi} J_2(x) \log\left(\frac{x}{2}\right) - \frac{4}{\pi x^2} - \frac{1}{\pi} - \frac{1}{\pi} \sum_{j=0}^{\infty} \frac{(-1)^j (\psi(j+1) + \psi(j+3))}{j!(j+2)!} \left(\frac{x}{2}\right)^{2j+2}, \quad (46)$$

where $\psi(\cdot)$ is the digamma function.

4.2. The kernel of S_k

For arbitrary wavenumber k and with r not necessarily on Γ we have

$$S_k(r, r') = \frac{i}{2} H_0^{(1)}(k|r - r'|). \quad (47)$$

Using (13) and (44) one can split $G(r, r') = S_k(r, r')$ in the form (43) with

$$G_L(r, r') = -\frac{1}{\pi} J_0(k|r - r'|), \quad (48)$$

$G_C = 0$, $G_H = 0$, and general limit

$$\lim_{r' \rightarrow r} G_0(r, r') = \frac{i}{2} - \frac{1}{\pi} (\log(k/2) - \psi(1)). \quad (49)$$

4.3. The kernel of K_k

For arbitrary wavenumber k and with r not necessarily on Γ we have

$$K_k(r, r') = \frac{i}{2} k|r - r'| H_1^{(1)}(k|r - r'|) D(r', r), \quad (50)$$

with $D(r', r)$ as in (15). In the limit of $k \rightarrow 0$ this means

$$K_0 \rho(r) = \frac{1}{\pi} \int_{\Gamma} D(r', r) \rho(r') d\ell' = -\Re \left\{ \frac{1}{\pi i} \int_{\Gamma} \frac{\rho(\tau) d\tau}{\tau - z} \right\}, \quad (51)$$

which is the Neumann–Poincaré operator with negative sign. Using (13) and (45) one can split $G(r, r') = K_k(r, r')$ in the form (43) with

$$G_L(r, r') = -\frac{1}{\pi} k|r - r'| J_1(k|r - r'|) D(r', r), \quad (52)$$

$$G_C(z, \tau) = -\frac{1}{\pi}, \quad (53)$$

$G_H = 0$, and general limit

$$\lim_{r' \rightarrow r} G_0(r, r') = 0. \quad (54)$$

For r on smooth Γ and with G_C as in (53), the third term on the right hand side of (43) is smooth and should be included in the first term. Then $G_C = 0$ and

$$\lim_{r' \rightarrow r} G_0(r, r') = \frac{(\nu \cdot \ddot{r})}{2\pi |\dot{r}|^2}, \quad (55)$$

where $\dot{r} = dr(s)/ds$ and $\ddot{r} = d^2r(s)/ds^2$.

Note that, thanks to k -independence in (53), the term associated with G_C in (43) cancels out in difference operators $K_{k_2} - K_{k_1}$.

4.4. The kernel of K_k^A

For arbitrary wavenumber k and with r not necessarily on Γ we have

$$K_k^A(r, r') = \frac{i}{2}k|r - r'|H_1^{(1)}(k|r - r'|)D(r, r'), \quad (56)$$

with $D(r, r')$ as in (15). In the limit of $k \rightarrow 0$ this means

$$K_0^A \rho(r) = \frac{1}{\pi} \int_{\Gamma} D(r, r') \rho(r') dl' = \Re \left\{ \frac{1}{\pi i} \int_{\Gamma} \frac{n_z \bar{n}_\tau \rho(\tau) d\tau}{\tau - z} \right\}. \quad (57)$$

Using (13) and (45) one can split $G(r, r') = K_k^A(r, r')$ in the form (43) with

$$G_L(r, r') = -\frac{1}{\pi}k|r - r'|J_1(k|r - r'|)D(r, r'), \quad (58)$$

$$G_C(z, \tau) = \frac{n_z \bar{n}_\tau}{\pi}, \quad (59)$$

$G_H = 0$, and general limit

$$\lim_{r' \rightarrow r} G_0(r, r') = 0. \quad (60)$$

For r on smooth Γ and with G_C as in (59), the third term on the right hand side of (43) is smooth and should be included in the first term. Then $G_C = 0$ and

$$\lim_{r' \rightarrow r} G_0(r, r') = \frac{(\nu \cdot \ddot{r})}{2\pi|\dot{r}|^2}. \quad (61)$$

4.5. The kernel of T_k

For arbitrary wavenumber k and with r not necessarily on Γ we have

$$\begin{aligned} T_k(r, r') &= \frac{i}{2}k|r - r'|H_1^{(1)}(k|r - r'|) \frac{(\nu \cdot \nu')}{|r - r'|^2} \\ &\quad + \frac{i}{2}(k|r - r'|)^2 H_2^{(1)}(k|r - r'|)D(r, r')D(r', r). \end{aligned} \quad (62)$$

Using (13) and (46) one can split $G(r, r') = T_k(r, r')$ in the form (43) with

$$\begin{aligned} G_L(r, r') &= -\frac{k}{\pi}J_1(k|r - r'|) \frac{(\nu \cdot \nu')}{|r - r'|} \\ &\quad - \frac{1}{\pi}(k|r - r'|)^2 J_2(k|r - r'|)D(r, r')D(r', r), \end{aligned} \quad (63)$$

$$G_C(z, \tau) = -\frac{k^2}{2\pi} \Re \{n_z(\bar{\tau} - \bar{z})\}, \quad (64)$$

$$G_H(z, \tau) = -\frac{n_z}{\pi}. \quad (65)$$

and general limit

$$\lim_{r' \rightarrow r} G_0(r, r') = \frac{i}{4}k^2 - \frac{1}{4\pi}k^2(2 \log(k/2) - 2\psi(1) - 1). \quad (66)$$

For r on smooth Γ and with G_C as in (64), the third term on the right hand side of (43) is smooth, has zero limit as $r' \rightarrow r$, and should be included in the first term. Then $G_C = 0$, but (66) is unaffected.

Note that, thanks to k -independence in (65), the term associated with G_H in (43) cancels out in difference operators $T_{k_2} - T_{k_1}$.

5. Existence and uniqueness of solutions

This section collects known results on the existence and the uniqueness of solutions to the PDE (3)–(8) and to the system of integral equations called KM0, KM1, and KM2 in Section 3.

5.1. Uniqueness: the PDE

According to the uniqueness theorem of [20, Section 2], if Γ is smooth, if $k_1 \neq 0$, and if (2) is assumed, a solution to (3)–(8) is unique if

$$0 \leq \arg(k_1) < \pi, \quad |\varepsilon| \neq \infty, \quad 0 \leq \arg(\varepsilon k_1) \leq \pi. \quad (67)$$

According to [22, Theorem 3.1], if Γ is smooth, if $k_1, k_2 \neq 0$, and if (2) is assumed, a solution to (3)–(8) is unique if

$$0 \leq \arg(k_1), \arg(k_2) \leq \pi/2 \quad \text{or} \quad \pi/2 \leq \arg(k_1), \arg(k_2) < \pi. \quad (68)$$

The two sets of conditions (67) and (68) overlap, but are not identical. For example, if $\arg(k_1) = \pi/2$ and $0 < \arg(k_2) < \pi/4$ then (68) holds but not (67) – a fact we think is due to a flaw in the proof of [22, Theorem 3.1] which affects the analysis of the solvability of [22, Eq. (4.5)]. In the present work we are chiefly interested in $\arg(k_1) = 0$, $0 \leq \arg(k_2) \leq \pi/2$. Then both (67) and (68) guarantee that a solution to (3)–(8) is unique if Γ is smooth.

5.2. Unique solvability: the systems of integral equations

According to [20, Theorem 4.1], if Γ is smooth, if (67) holds, and if c is as in (24), then the KM1 system (25) is uniquely solvable. The unique solution μ, ρ gives, via (22) and (23), a unique solution to (3)–(8). As a consequence, the KM0 system and the Müller-Rokhlin equations, which correspond to the KM1 system with $c = 1$, are also uniquely solvable if both k_1 and k_2 are real and positive. In our numerical experiments with KM1 in Section 9, where $\Re\{k_1\} \geq 0$, we choose c in accordance with (24) as

$$c = \varepsilon k_2 / |\varepsilon k_2|. \quad (69)$$

According to [20, Theorems 4.2 and 4.3], if Γ is smooth and if both k_1 and k_2 are real and positive, then the KM2 system (32) is uniquely solvable. The solution gives, via (28) and (29), a unique solution to (3)–(8).

5.3. True and false eigenwavenumbers

When k_1 and ε are such that the conditions (67) are violated, a solution to (3)–(8) may, or may not, be unique. The same applies to solutions to the systems of integral equations of Section 3 if the conditions on unique solvability of Section 5.2 are violated.

Assume now that the conditions on unique solvability of Section 5.2 are violated for a given system of integral equations in Section 3. If, for some k_1 and ε , we numerically detect a non-trivial homogeneous solution to that system, we call k_1 an *eigenwavenumber*. Eigenwavenumbers can be of two types: those that correspond to non-vanishing eigenfields $U(r)$ that satisfy the boundary conditions (5) and (6) and those that correspond to $U(r) = 0$ or violate the boundary condition (5). We call the former type *true eigenwavenumbers* and the latter type *false eigenwavenumbers*. False eigenwavenumbers that correspond to eigenfields that violate (5) can only occur for the KM2 equations since $U(r)$ in the KM0 and KM1 equations, by construction, always satisfies (5).

5.4. Existence: the KM1 system on a boundary with corners

This section discusses some issues related to the existence of solutions to the KM1 system (25) when Γ has corners, ε is close to or on the negative real axis, and k_1 is real and positive so that $c \approx -i$ according to (69).

In view of the singular nature of the kernels of the integral operators in Section 4, and when $r \in \Gamma$, the KM1 system can be written in the form

$$\begin{bmatrix} I + \lambda_1 K_0 + C_1 & C_2 \\ C_3 & I + \lambda_2 K_0^A + C_4 \end{bmatrix} \begin{bmatrix} \mu(r) \\ \rho(r) \end{bmatrix} = \begin{bmatrix} f_1(r) \\ f_2(r) \end{bmatrix}, \quad (70)$$

where C_1, C_2, C_3 , and C_4 are compact integral operators on Γ also in the presence of corners, K_0 and K_0^A are as in (51) and (57), and

$$\lambda_1 = \frac{1 - \varepsilon}{1 + \varepsilon}, \quad \lambda_2 = \frac{c - \varepsilon}{c + \varepsilon}. \quad (71)$$

The operators K_0 and K_0^A are singular bounded integral operators on Γ . The operator K_0^A is the same as the operator denoted K in [15, Eq. (10)].

The system (70) is a compact perturbation of the de-coupled system

$$\begin{bmatrix} I + \lambda_1 K_0 & 0 \\ 0 & I + \lambda_2 K_0^A \end{bmatrix} \begin{bmatrix} \mu(r) \\ \rho(r) \end{bmatrix} = \begin{bmatrix} f_1(r) \\ f_2(r) \end{bmatrix}, \quad (72)$$

whose spectral properties, including the essential spectrum of K_0 and K_0^A in planar domains with corners, have been analyzed in [24].

In particular, when Γ has a corner with opening angle θ and when ε of (71) is real and such that

$$-\left|1 - \frac{\theta}{\pi}\right| < -\frac{1}{\lambda_1} < \left|1 - \frac{\theta}{\pi}\right| \Leftrightarrow \frac{|\pi - \theta| + \pi}{|\pi - \theta| - \pi} < \varepsilon < \frac{|\pi - \theta| - \pi}{|\pi - \theta| + \pi}, \quad (73)$$

then (72) does not in general have a solution μ in the fractional Sobolev space $H^{1/2}(\Gamma)$, see [6], corresponding to boundary values of potentials with finite absolute energy in the sense of [15, Section 4]. There exists, however, a solution $\mu \in H^{1/2}(\Gamma)$ for λ_1 arbitrarily close to, but not on, the real axis. We remark that similar restrictions on the solvability of (72) apply to ρ if $-1/\lambda_2$ is real and in the interval specified by (73). Since, by assumption on ε and k_1 , the parameter λ_2 of (71) is not close to the real axis and we disregard this possibility.

The essential spectrum of an integral operator is invariant under compact perturbations. Therefore the solvability analysis for (72) also applies to (70). When (73) holds in our numerical examples of Section 9, we then add a small imaginary number $i\delta$, $\delta > 0$, to ε and solve (70) in the limit $\delta \rightarrow 0^+$. This corresponds to λ_1 approaching the real axis from below in the complex plane. The limit solutions are indicated with a plus-sign superscript.

6. The Drude model and surface plasmon waves

We are interested in wave phenomena which under certain conditions appear in metallic objects with sharp edges. Let us assume that there is vacuum in Ω_1 , that k_1 is real and positive, and that Ω_2 is a metal. Certain metals, such as silver, have permittivities that often are well approximated by the Drude model, see [19, Eq. (7.58)], which in our context reads

$$\varepsilon = 1 - \frac{k_p^2}{k_1^2 + ik_1\gamma}. \quad (74)$$

Here k_p is the plasma wavenumber and $\gamma \geq 0$ is a damping constant. The equation says that ε becomes real and negative when $k_1 < k_p$ and $\gamma \rightarrow 0^+$. We mention the Drude model merely to explain why real and negative ε can occur for real and positive k_1 .

When ε is real the time average of the electric and the magnetic energy densities, normed by the vacuum permeability, are

$$\langle w_{\text{el}}(r) \rangle = \frac{1}{4k_i^2} |\nabla U(r)|^2, \quad r \in \Omega_i, \quad i = 1, 2, \quad (75)$$

$$\langle w_{\text{ma}}(r) \rangle = \frac{1}{4} |U(r)|^2, \quad r \in \mathbb{R}^2. \quad (76)$$

This means that if $\varepsilon < 0$, then $\langle w_{\text{el}}(r) \rangle$ is negative inside Ω_2 while $\langle w_{\text{ma}}(r) \rangle$ is positive and electromagnetic waves cannot propagate in Ω_2 . It is, however, possible for so-called *surface plasmon waves* to propagate in a direction along Γ . This is illustrated in the numerical examples of Section 9.5, below, where surface plasmon waves are excited and propagate along Γ of a bounded object. The properties of these waves resemble those of surface plasmon waves along planar surfaces, and this resemblance is enhanced as the wavelength of the surface plasmon waves decreases.

The main results for surface plasmon waves on planar surfaces, pertinent also for curved Γ , are as follows, see [25, Appendix I]: The surface plasmon waves can occur only for $\varepsilon < -1$, they are evanescent (which roughly means exponentially decaying) in directions perpendicular to Γ , and propagate along Γ with wavenumber

$$k_{\text{sp}} = k_1 \sqrt{\frac{|\varepsilon|}{|\varepsilon| - 1}}, \quad \varepsilon < -1. \quad (77)$$

Surface plasmon waves can always propagate when $\varepsilon < -1$ and $k_1 > 0$, but their excitation by an incident wave $U^{\text{in}}(r)$ requires special couplers or that Γ is somehow rough [25, Sections 2.2 and 6.7]. Surface plasmon waves are particularly easy to excite when Γ has corners and ε is infinitely close to the interval where (73) holds. That is, when ε approaches the interval

$$\frac{|\pi - \theta| + \pi}{|\pi - \theta| - \pi} < \varepsilon < -1 \quad (78)$$

from above in the complex plane. Note that, in (77), the wavenumber k_{sp} diverges as $\varepsilon \rightarrow -1^-$. More details on surface plasmon waves can, for example, be found in [2, 27]. Their excitation by corners is the topic of the next section.

7. Singular fields at corners

The presence of corners on Γ has a great influence on the excitation of surface plasmon waves and, as a consequence, on scattering and absorption cross sections. The mechanism behind this is governed by certain singular eigenfields which can be determined by quasi-static analysis, see [5]. We now briefly review some results on this topic.

7.1. Quasi-static eigenfields

In the limit $k_1 \rightarrow 0$ and for certain ε , the transmission problem of Section 2 can allow for magnetic eigenfields. These eigenfields are non-trivial solutions to

$$\Delta U(r) = 0, \quad r \in \Omega_1 \cup \Omega_2, \quad (79)$$

$$\lim_{\Omega_1 \ni r \rightarrow r^\circ} U(r) = \lim_{\Omega_2 \ni r \rightarrow r^\circ} U(r), \quad r^\circ \in \Gamma, \quad (80)$$

$$\lim_{\Omega_1 \ni r \rightarrow r^\circ} \varepsilon \nu^\circ \cdot \nabla U(r) = \lim_{\Omega_2 \ni r \rightarrow r^\circ} \nu^\circ \cdot \nabla U(r), \quad r^\circ \in \Gamma, \quad (81)$$

$$\lim_{|r| \rightarrow \infty} U(r) = 0, \quad r \in \Omega_1, \quad (82)$$

and they are important in the analysis of cross sections of objects Ω_2 that are much smaller than the wavelength $2\pi/k_1$.

It follows from (79)–(82) that the eigenfields have zero electric energy when $\Im\{\varepsilon\} = 0$, that is,

$$\int_{\Omega_1} |\nabla(U(r))|^2 dS + \frac{1}{\varepsilon} \int_{\Omega_2} |\nabla(U(r))|^2 dS = 0, \quad (83)$$

where dS is an element of area.

An alternative and, perhaps, more common analysis uses the scalar electric potential $V(r)$, related to $\mathbf{E}(r)$ of (12) via $\mathbf{E}(r) = -\nabla V(r)$. The eigenproblem for $V(r)$ is the same as that for $U(r)$ but with ε replaced by $1/\varepsilon$ in the quasi-static boundary condition (81) and in (83). Since $U(r)$ and $V(r)$ give rise to the same electric field we have

$$\nabla V(r) = \begin{cases} A\nabla U(r) \times \hat{\mathbf{z}}, & r \in \Omega_1, \\ A\varepsilon^{-1}\nabla U(r) \times \hat{\mathbf{z}}, & r \in \Omega_2, \end{cases} \quad (84)$$

where A is a normalization constant. The quasi-static potentials $U(r)$ and $V(r)$ are still complex representations of physical fields via (9) and $V(r, t) = \Re\{V(r)e^{-it}\}$.

7.2. Eigenfields of the semi-infinite wedge

Magnetic and electric eigenfields can, in the limit $k_1 \rightarrow 0$, only occur when ε is real and negative. When Γ is smooth there is a discrete set of ε that admits eigenfields. When Γ is the open boundary of a semi-infinite wedge of opening angle θ there exist eigenfields for all ε that satisfy (73). These wedge eigenfields satisfy (79)–(81) and (83), but not (82), and are often used in the static analysis of singular fields in domains containing finite non-smooth objects. See [3] for a rigorous justification of this practice.

The wedge eigenfields describe the singular fields that can arise at corners of a finite object Ω_2 . They shed light on how incident waves can couple very strongly to surface plasmon waves and affect scattering and absorption cross sections of objects for all wavenumbers k_1 . Let ϕ be the azimuth angle and let Γ be given by $\phi = \pm\theta/2$. Then the wedge eigenfields can be found via separation of variables and have the form

$$U(r) = |r|^{\pm i\zeta} \Theta(\phi), \quad (85)$$

where ζ is a real and positive parameter that solves a transcendental equation [5, Section 3]. The function $\Theta(\phi)$ is odd or even depending on whether $\varepsilon < -1$ or $\varepsilon > -1$.

The gradients $\nabla U(r)$ of the wedge eigenfields (85) make both integrals in (83) divergent. The time-average power loss (absorbed power) inside a disk of radius R , centered at the corner vertex of the wedge, is proportional to

$$\lim_{\Im\{\varepsilon\} \rightarrow 0^+} \Im\{\varepsilon\} \int_{S_w} |\nabla(U(r))|^2 dS, \quad (86)$$

where S_w is the part of the disk that overlaps the wedge. The limit in (86) is non-zero and independent of $R > 0$. This means that power is absorbed by the wedge even though it becomes lossless as $\Im\{\varepsilon\} \rightarrow 0^+$. A quasi-static analysis shows that Poynting's theorem [23, Section 1.3.3] is satisfied. The power absorption is located in a disk with an infinitesimally small R and is equal to the time-average power flow through the boundary of a disk with arbitrarily large R . A detailed analysis shows that, for the wedge eigenfields in (85), this power absorption depends strongly on ε . It goes to zero as $\varepsilon \rightarrow -1$, but is otherwise positive.

7.3. Coupling to surface plasmon waves

The plane wave excitation of surface plasmon waves along a boundary Γ with a corner can, heuristically, be explained as follows: $U^{\text{in}}(r)$ induces a magnetic field in the vicinity of the corner that we refer to as a *corner field*. The corner field resembles the wedge eigenfields (85). According to (9), the time-harmonic magnetic wedge eigenfield associated with (85) is

$$H(r, t) = \Theta(\phi) \cos(\zeta \log |r| \pm t). \quad (87)$$

This eigenfield can be viewed as a wave that travels radially inwards ($+t$) or outwards ($-t$) with a local wavelength, $2\pi|r|/\zeta$, that increases linearly with $|r|$. The corresponding time-harmonic corner field inherits these characteristics. At the value of $|r|$ where the local wavelength equals the wavelength of the surface plasmon waves, $2\pi/k_{\text{sp}}$ see (77), the corner field couples to the surface plasmon waves on Γ . Only odd corner fields can couple to surface plasmon waves since the latter only exist for $\varepsilon < -1$, see Section 6.

8. Cross sections

With the incident plane wave $U^{\text{in}}(r)$ of (1), the scattering cross section, σ_{sc} , and the absorption cross section, σ_{abs} , of Ω_2 are defined as time averages of the scattered and absorbed power densities divided by the time average of the incident power density. Let Γ_C be a contour enclosing Ω_2 and with outward unit normal ν . Then [23, Section 4.2]

$$\sigma_{\text{sc}} = \Im \left\{ \frac{1}{k_1} \int_{\Gamma_C} (\nu \cdot \nabla U^{\text{sc}}(r)) \overline{U^{\text{sc}}(r)} \, d\ell \right\}, \quad (88)$$

$$\sigma_{\text{abs}} = -\Im \left\{ \frac{1}{k_1} \int_{\Gamma_C} (\nu \cdot \nabla U(r)) \overline{U(r)} \, d\ell \right\}. \quad (89)$$

When the object has corners and the real part of ε is negative, the absorption cross section can be positive, even in the limit of the imaginary part of ε going to zero. The absorption can be explained by the quasi-static analysis in Section 7 and is verified numerically in Section 9.7.

The total cross section in the direction d of $U^{\text{in}}(r)$ is

$$\sigma_{\text{tot}} = \sigma_{\text{sc}} + \sigma_{\text{abs}}. \quad (90)$$

The optical theorem, [19, Section 10.11], [23, Section 4.4], gives the alternative expression for the total cross section

$$\sigma_{\text{tot}} = - \lim_{|r| \rightarrow \infty} \Im \left\{ \frac{4}{k_1} U^{\text{sc}}(|r|d) \sqrt{\frac{\pi k_1 |r|}{2}} e^{-i(k_1 |r| - \pi/4)} \right\}. \quad (91)$$

9. Numerical examples

In a series of progressively more challenging problems we now put the integral equations of Section 3 and the discretization techniques of Section 4 to the test. Only a few of our problems have (semi-)analytic solutions. When assessing the accuracy of computed quantities we therefore often adopt a procedure where to each numerical solution we also compute an overresolved reference solution, using roughly 50% more points in the discretization of the integral equations. The absolute difference between these two solutions is denoted the *estimated absolute error*.

Our codes are implemented in MATLAB, release 2016b, and executed on a workstation equipped with an Intel Core i7-3930K CPU. The implementations are standard, rely on built-in functions, and include a few `parfor`-loops (which execute in parallel).

9.1. Numerical tests of integral operators

The operators S_k , K_k , K_k^{A} and T_k , $r \in \Gamma$, have been implemented on the “star” boundary [8, 12] parameterized as

$$r(s) = \frac{9}{20} \left(1 + \frac{20}{81} \sin(5s) \right) (\cos(s), \sin(s)), \quad -\pi \leq s \leq \pi. \quad (92)$$

Product integration weights for kernels with logarithmic singularities are computed using analytical methods and recursion [12, Appendix A], while local regularization [9, Section 2.2] is used for hypersingular kernels.

The compositions of operators $K_k K_k - S_k T_k$ and $K_k^{\text{A}} K_k^{\text{A}} - T_k S_k$ act as the identity operator on simple smooth layer densities, compare (20) and (21). For example, with $k = 3.8 + 1.3i$, $f(r(s)) = \cos(3s) + i \sin(7s)$, and 384 discretization points on Γ of (92), the relation $(K_k K_k - S_k T_k)f(r) = f(r)$ holds with a relative accuracy of $4 \cdot 10^{-15}$ in L^2 -norm. With 1152 discretization points, the relation $(K_k^{\text{A}} K_k^{\text{A}} - T_k S_k)f(r) = f(r)$ holds with a relative accuracy of $4 \cdot 10^{-14}$.

Table 1: Estimates of true and false eigenwavenumbers of the KM0 and KM2 systems for the unit circle with $\varepsilon = 2.25$.

k_1	multiplicity	nature
2.380109395443269 – 0.303953834460040i	simple	false
3.041565475205771 – 1.041465761622153i	double	true
3.815540575399378 – 0.309076450175921i	double	false
4.892032383544720 – 0.631231166352111i	double	true

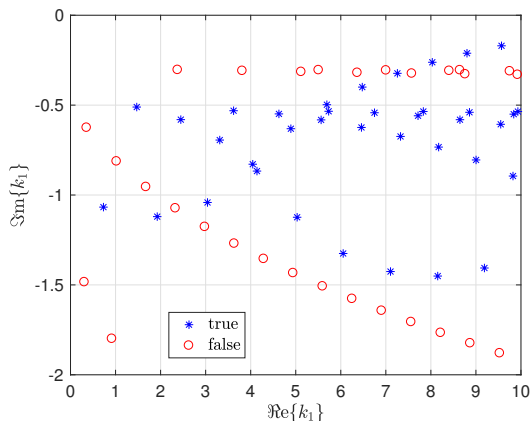


Figure 1: True and false eigenwavenumbers k_1 of the KM0 and KM2 systems for the unit circle with $\varepsilon = 2.25$.

9.2. Eigenwavenumbers for the unit circle

We first choose $\varepsilon = 2.25$ so that $\arg(k_1) = \arg(k_2)$, let Γ be the unit circle, and look for true and false eigenwavenumbers k_1 with $\Re\{k_1\} > 0$ using 352 discretization points on Γ . We investigate the KM0 system, which is (25) with $c = 1$, and the KM2 system (32). See Section 5.3 for the definition of true and false eigenwavenumbers.

As it turns out in our numerical experiments, the eigenwavenumbers of the KM0 system and those of the KM2 system are the same. A few examples are listed in Table 1. The true eigenwavenumbers are confirmed to a relative precision of $4 \cdot 10^{-16}$ by comparison with semi-analytic results, computed as solutions to transcendental equations derived in analogy with their three-dimensional counterparts in [22, Section 3]. We believe that this precision is indicative of the precision in all computed eigenwavenumbers in this and the following sections. Figure 1 illustrates all eigenwavenumbers found with $0 \leq \Re\{k_1\} \leq 10$ and $\Im\{k_1\} \geq -2$. The eigenwavenumbers are found using a combination of brute-force random search and Broyden's method, see [14, Section VI.B] for a few more details. No eigenwavenumber has $\Im\{k_1\} \geq 0$, in agreement with the theory of Section 5.2.

We then choose $\varepsilon = -1.1838$, which is used in [5]. The condition numbers of the matrices resulting from discretization of the KM1 system and the KM0

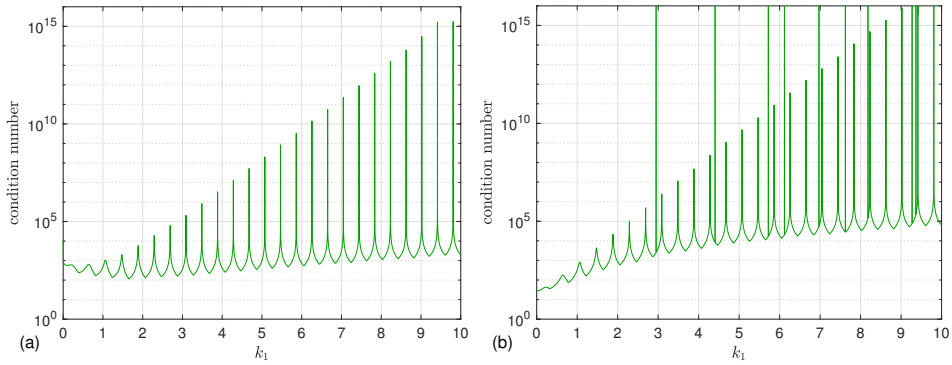


Figure 2: Condition numbers of system matrices from the KM1 and the KM0 systems for the unit circle, $\varepsilon = -1.1838$, and $k_1 \in [0, 10]$: (a) the KM1 system is free of false eigenwavenumbers; (b) the KM0 system exhibits nine false eigenwavenumbers.

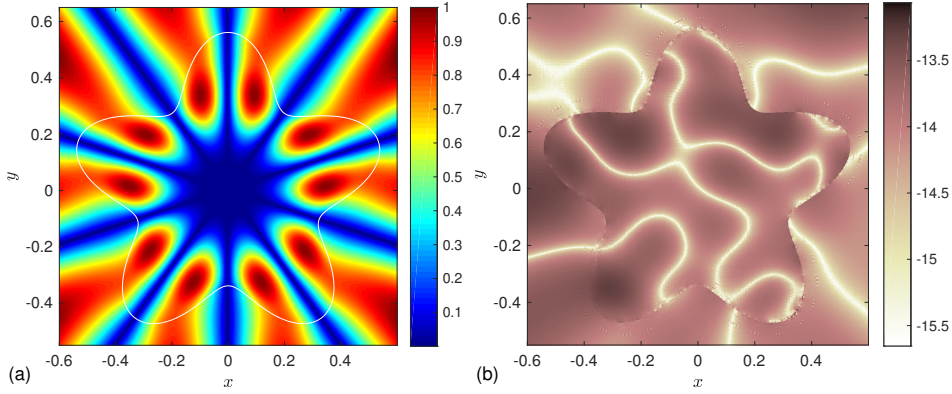


Figure 3: Normalized eigenfield $U(r)$ for Γ of (92) and with $\varepsilon = 2.25$ and estimated eigenwavenumber $k_1 = 13.21401616284493 - 1.636497767435982i$: (a) absolute field value $|U(r)|$; (b) \log_{10} of estimated absolute field error in $|U(r)|$.

system are studied as a function of $k_1 \in [0, 10]$ using 384 discretization points on Γ . Note that KM1, according to (69), now has $c = -i$ while KM0 always corresponds to $c = 1$, so the two systems are not the same. Figure 2(a) shows that the KM1 system does not exhibit any false eigenwavenumber, in agreement with the theory of Section 5.2. The KM0 system exhibits nine false eigenwavenumbers, see Figure 2(b). Furthermore, the KM1 system leads to generally better conditioned matrices. The sharp peaks that are common to Figures 2(a) and 2(b) are caused by eigenwavenumbers close to, but below, the real k_1 -axis. Results for the KM2 system (not shown) are very similar to those of the KM0 system: the false eigenwavenumbers are the same, but the condition numbers are generally slightly smaller.

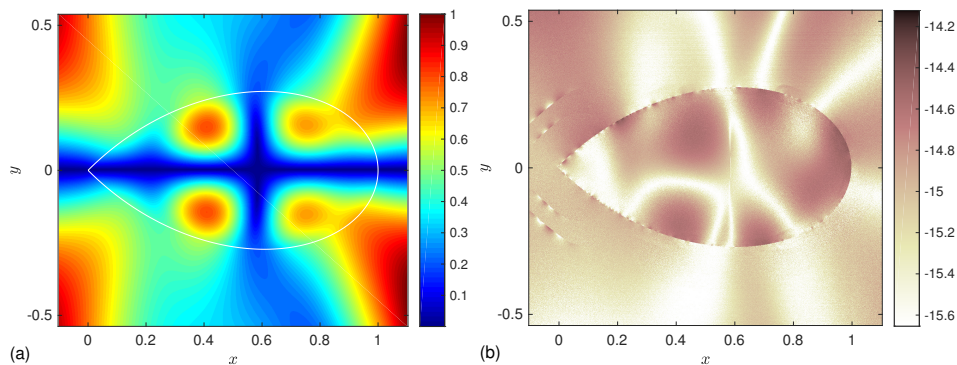


Figure 4: Normalized eigenfield $U(r)$ for Γ of (93) and with $\varepsilon = 2.25$ and estimated eigenwavenumber $k_1 = 9.701129417644246 - 2.000374579086419i$: (a) absolute field value $|U(r)|$; (b) \log_{10} of estimated absolute field error in $|U(r)|$.

9.3. Eigenfield for a “star”

We choose $\varepsilon = 2.25$ for the “star” of (92), again look for non-trivial solutions to the homogeneous KM0 system, and then compute eigenfields $U(r)$ via (22) and (23) at 10^6 field points placed on a Cartesian grid in the box $\mathcal{B} = \{-0.6 \leq x \leq 0.6, -0.55 \leq y \leq 0.65\}$. The eigenfields are normalized with their largest value in \mathcal{B} .

Figure 3 shows the eigenfield for the simple estimated eigenwavenumber $k_1 = 13.21401616284493 - 1.636497767435982i$ along with the estimated absolute field-error computed with 976 discretization points on Γ . The accuracy is very high, also close to Γ , which demonstrates the power of the near-boundary evaluation scheme of Section 4.

9.4. Eigenfield for a one-corner object

We now let Γ be a closed contour with one corner, parameterized as

$$r(s) = \sin(\pi s) (\cos((s - 0.5)\theta), \sin((s - 0.5)\theta)), \quad 0 \leq s \leq 1. \quad (93)$$

We choose $\varepsilon = 2.25$ and $\theta = \pi/2$ and repeat the experiment of Section 9.3 with the KM0 system. RCIP acceleration is activated due to the presence of the corner, see Section 4, and 320 discretization points are placed on the coarse mesh on Γ . Figure 4 shows the eigenfield for the simple estimated eigenwavenumber $k_1 = 9.701129417644246 - 2.000374579086419i$ along with the estimated absolute error at 10^6 field points. The accuracy is even higher than in the example of Section 9.3, which demonstrates the power of RCIP and that boundary value problems on domains with corners are not necessarily more difficult to solve than boundary value problems on smooth domains.

9.5. Surface plasmon wave for a one-corner object

We solve the KM1 equations with $\varepsilon = -1.1838$, $k_1 = 18$, Γ as in (93), $\theta = \pi/6$, and $U^{\text{in}}(r)$ as in (1) with $d = (\cos(5\pi/12), \sin(5\pi/12))$. This setup is chosen as to create a surface plasmon wave and to resemble the setup of [5, Section 4.4.1].

The KM1 system (70), which now has $c = -i$ according to (69), is solved for the limit solution μ^+ , ρ^+ . The representations (22) and (23) are used for $U^+(r)$ and (9) is used for $H^+(r, 0)$. Some resolution issues, related to the relatively small opening angle $\theta = \pi/6$ and quadrature panels on opposing sides of the corner vertex lying close to each other, require that the number of points used in the underlying quadrature is increased from $n_{\text{pt}} = 16$ to $n_{\text{pt}} = 22$. Compare [11, Section 21.1].

Figure 5 shows a sequence of zooms of $H^+(r, 0)$ in the vicinity of the corner vertex, along with a plot of the estimated absolute field error. There are 1100 discretization points on the coarse mesh on Γ and each computational box contains 10^6 field points on a (rectangular) Cartesian grid. According to the analysis of Section 6, a surface plasmon wave can propagate along Γ with a wavelength $2\pi/k_{\text{sp}} \approx 0.138$. Figure 5(a) shows that this indeed happens. An animation of a surface plasmon wave $H^+(r, t)$, $t \in [0, 2\pi]$, along Γ can be found in [18].

The estimated field accuracy is not affected by the proximity of a field point to the corner vertex, as shown in Figures 5(b,d,f). At least thirteen digits can be obtained irrespective of the level of zoom. Figure 5(a,c,e) can serve as an illustration to the discussion in Section 7.3 of how the odd magnetic eigenfields (87) couple to the surface plasmon waves.

9.6. Fields and gradient fields

We compare the performance of the KM1 equations to the performance of the KM2 equations where (37) is used for field evaluations at points r close to Γ .

The first setup has $\varepsilon = 2.25$, $k_1 = 18$, Γ as in (93), $\theta = \pi/2$, U^{in} as in (1), and $d = (\cos(\pi/4), \sin(\pi/4))$. (Recall that with both ε and k_1 real and positive, $c = 1$ in (69) and the KM1 equations coincide with the KM0 equations). Both the field $H(r, 0)$ and the gradient field $\nabla H(r, 0)$ are computed. Figure 6 shows that the achievable accuracy in $H(r, 0)$ and $\nabla H(r, 0)$ is improved with around one and three digits, respectively, when the KM2 system with (37) is used rather than the KM1 equations. There are 800 discretization points on the coarse mesh on Γ and 10^6 field points on a (rectangular) Cartesian grid in the box $\mathcal{B} = \{-0.1 \leq x \leq 1.1, -0.54 \leq y \leq 0.54\}$.

Figure 7 shows results for a second setup with $\varepsilon = -1.1838$, the geometry and the mesh being the same as above. We only use the KM1 equations, with $c = -i$ according to (69). The surface plasmon wavelength of $2\pi/k_{\text{sp}} \approx 0.138$ corresponds to 17.6 wavelengths along Γ – a number that agrees well with

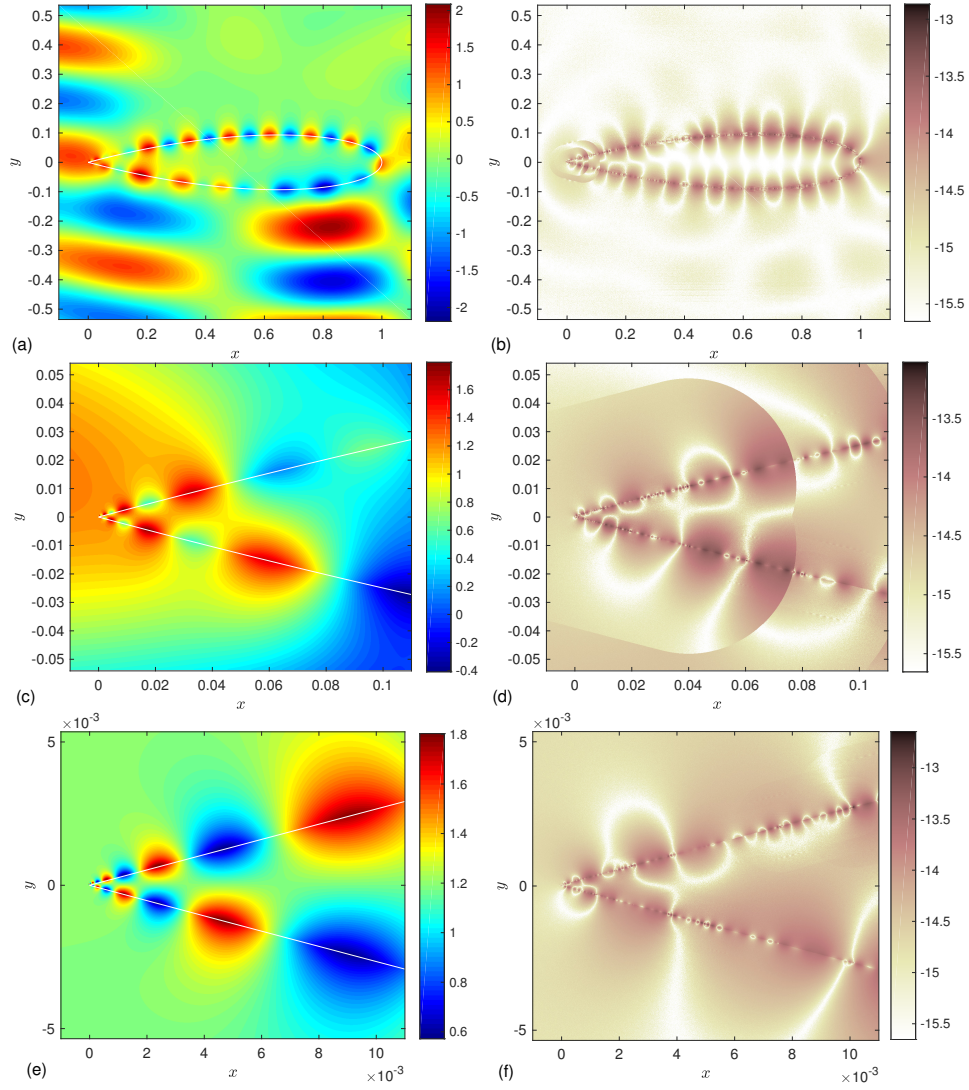


Figure 5: A corner zoom for $\varepsilon = -1.1838$, Γ as in (93), $\theta = \pi/6$, $k_1 = 18$, and $d = (\cos(5\pi/12), \sin(5\pi/12))$: (a,b) $H^+(r, 0)$ of (9) and \log_{10} of estimated absolute error; (c,d) ten times magnification; (e,f) 100 times magnification.

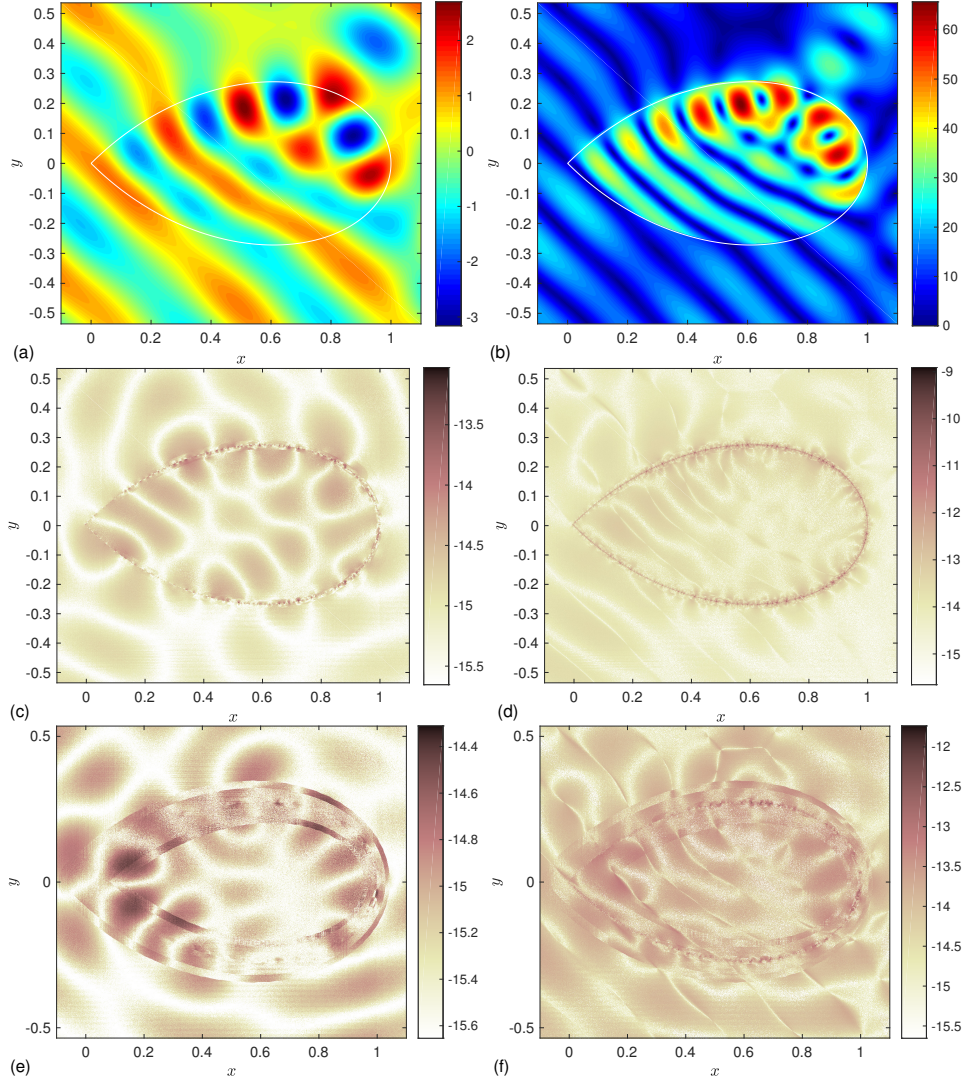


Figure 6: $H(r,0)$ and $\nabla H(r,0)$ with $k_1 = 18$, $\varepsilon = 2.25$, $\theta = \pi/2$, and $d = (\cos(\pi/4), \sin(\pi/4))$; (a) The field $H(r,0)$; (b) The field $|\nabla H(r,0)|$; (c) \log_{10} of estimated absolute error in $H(r,0)$ with KM1; (d) \log_{10} of estimated absolute error in $|\nabla H(r,0)|$ with KM1; (e) \log_{10} of estimated absolute error in $H(r,0)$ with KM2 and (37); (f) \log_{10} of estimated absolute error in $|\nabla H(r,0)|$ with KM2 and (37).

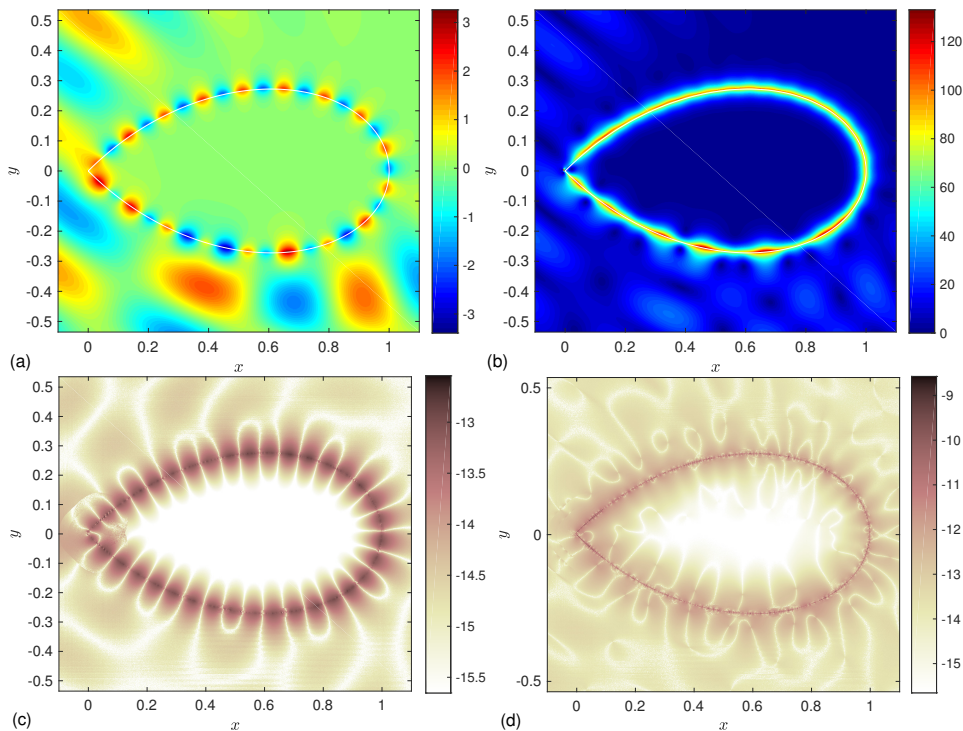


Figure 7: $H^+(r,0)$ and $\nabla H^+(r,0)$ with $k_1 = 18$, $\varepsilon = -1.1838$, $\theta = \pi/2$, and $d = (\cos(\pi/4), \sin(\pi/4))$: (a) The field $H^+(r,0)$; (b) The (diverging) field $|\nabla H^+(r,0)|$ with colorbar range set to $[0, 133]$; (c) \log_{10} of estimated absolute error in $H^+(r,0)$ with KM1; (d) \log_{10} of estimated absolute error in $|\nabla H^+(r,0)|$ with KM1.

the wave pattern of Figure 7(a). Note that the gradient field $\nabla H^+(r,0)$ of Figure 7(b) diverges in the corner and that the colorbar range is limited to $[0, 133]$ as to provide full dynamic color range away from the corner. The absolute gradient field error shown in Figure 7(d) corresponds to ten digit accuracy or better.

We end this section with some timings for the computations used to produce Figure 7(a): setting up the discretized KM1 system matrix took 4.3 seconds; constructing the compressed weighted inverse used for RCIP acceleration took 23 seconds; solving the main linear system took 0.25 seconds; evaluating $H^+(r,0)$ took, on average, 0.6 milliseconds per field point in \mathcal{B} .

9.7. The absorption cross section

We compute the limit absorption cross section σ_{abs}^+ of (89) for a scatterer with Γ as in (93), $\theta = \pi/2$, $d = (\cos(\pi/4), \sin(\pi/4))$, $k_1 = 18$, $\varepsilon < 0$, and Γ_C as the unit circle centered at $r = 0.5$. The KM1 equations are used, with $c = -i$ according to (69). Figure 8 shows results for σ_{abs}^+ , for a quantity that is machine epsilon ϵ_{mach} times the condition number κ of the system matrix, for the estimated absolute error in σ_{abs}^+ and, as a consistency check,

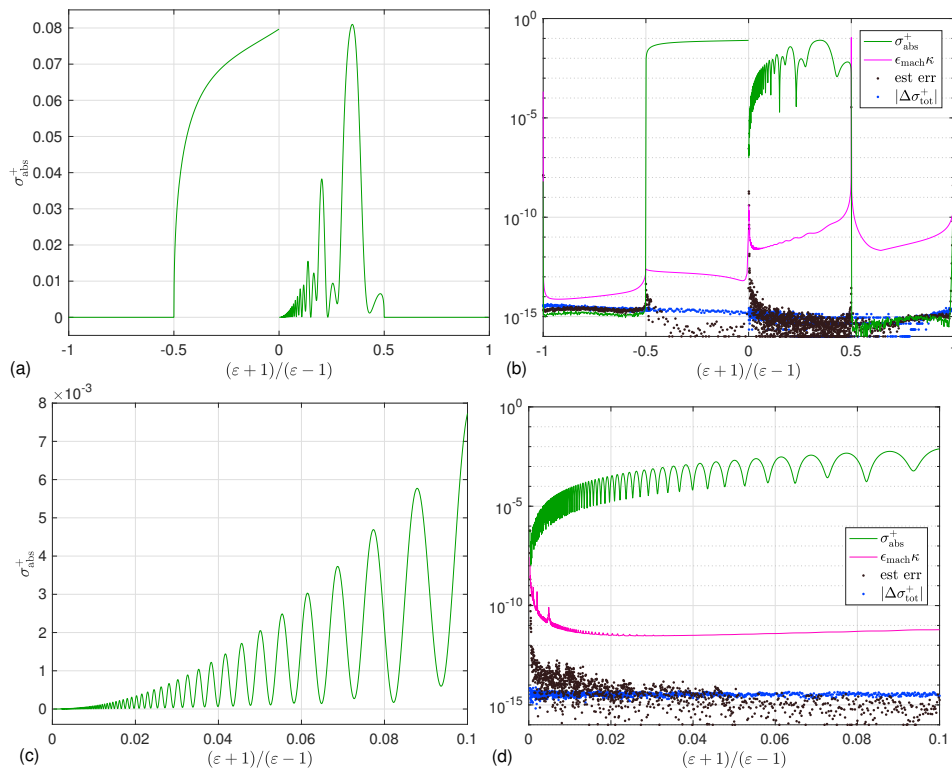


Figure 8: The absorption cross section σ_{abs}^+ of (89) of an object with Γ as in (93), $\theta = \pi/2$, $d = (\cos(\pi/4), \sin(\pi/4))$, $k_1 = 18$, and $\varepsilon < 0$: (a) σ_{abs}^+ ; (b) σ_{abs}^+ , $\varepsilon_{\text{mach}}\kappa$ times the condition number κ , estimated absolute error in σ_{abs}^+ , and the absolute difference of σ_{tot}^+ from (90) and from (91) with logarithmic scale on the y -axis; (c,d) higher resolution of (a,b) in the interval $0 < (\varepsilon + 1)/(\varepsilon - 1) \leq 0.1$.

for the absolute difference between σ_{tot}^+ computed from (90) and from (91).

The curves in Figure 8(a,b) are resolved by 1839 different values of ε , 1280 discretization points on the coarse mesh on Γ , and with $n_{\text{pt}} = 16$ in the underlying quadrature. The magnified curves in Figure 8(c,d) use 1239 different values of ε , 2560 discretization points on the coarse mesh, and $n_{\text{pt}} = 32$. One can see that the condition number of the discretized KM1 system is low for most values of ε , with the exception of values that make $(\varepsilon + 1)/(\varepsilon - 1)$ belong to the set $\{-1, 0, 0.5\}$.

Figure 8(d) also shows that high accuracy in σ_{abs}^+ requires at least ten discretization points per surface plasmon wavelength and that it is not enough to merely resolve the incident plane wave. For example, with $(\varepsilon + 1)/(\varepsilon - 1) = 6 \cdot 10^{-4}$, which corresponds to about 200 surface plasmon wavelengths along Γ and 12.8 discretization points per surface plasmon wavelength on the coarse mesh, the estimated absolute error in σ_{abs}^+ is around 10^{-12} . Smaller values of $(\varepsilon + 1)/(\varepsilon - 1)$ give a much larger error since the number of discretization points in Figure 8(c,d) is fixed while the surface plasmon wavelength $2\pi/k_{\text{sp}}$

decreases with $(\varepsilon + 1)/(\varepsilon - 1)$.

The rapid variations in σ_{abs}^+ for $0 < (\varepsilon + 1)/(\varepsilon - 1) < 0.5$, seen in Figure 8, are due to the coupling between corner fields and surface plasmon waves. For $-0.5 < (\varepsilon + 1)/(\varepsilon - 1) < 0$ there are no surface plasmon waves and σ_{abs}^+ varies less. The general behavior of σ_{abs}^+ in Figure 8 can be explained using an analytic expression for the absorbed power of the wedge eigenfields, obtained by inserting (85) into (86), multiplied with the squared amplitudes of the numerically determined corner fields.

10. Conclusions

The mathematical and physical theory behind the excitation of surface plasmon waves in finite metallic objects with sharp edges by incident plane waves is rather involved. The present work demonstrates that a robust integral equation-based solver for the underlying Helmholtz transmission problem can be constructed and used for the detailed study of surface plasmon waves in difficult situations. The solver combines a system of integral equations due to Kleinman and Martin, called KM1 in the present work, with mildly modified off-the-shelf numerical tools such as Nyström discretization, RCIP acceleration, and a product integration scheme for the evaluation of layer potentials. No assumptions about the solution are needed beyond those that are explicit in the PDE formulation of the problem. Corner fields and surface plasmon waves can be computed very accurately and that is crucial for the evaluation and understanding of rapidly varying absorption cross sections.

The KM1 system contains a parameter c , which should be chosen in agreement with (24). A choice of c in agreement with (24) makes the KM1 system uniquely solvable on smooth boundaries Γ under plasmonic conditions (the incident wavenumber k_1 is real and positive and the permittivity ratio ε is real and negative) and when the underlying transmission problem has a unique solution. Furthermore, when Γ has corners and ε is close to (but not on) an interval on the negative real axis where solutions do not exist, this choice of c makes one of the layer densities of the KM1 system (denoted ρ in the present work) particularly easy to resolve numerically.

As a “take-home message” one can say that it is important to choose c in agreement with (24) for the KM1 system. The choice $c = 1$, which is common in the literature and gives the KM0 equations of the present work, is only guaranteed to be good when k_1 and ε both are real and positive. On the other hand, under such conditions the equations called KM2 in the present work are preferable. The KM2 and KM0 systems have similar spectral properties, but the KM2 representation of the total magnetic field U lends itself better to accurate field evaluation close to Γ than does the representation of U in the KM0 equations.

Acknowledgement

This work was supported by the Swedish Research Council under contract 621-2014-5159.

References

- [1] L. af Klinteberg and A.-K. Tornberg. Adaptive quadrature by expansion for layer potential evaluation in two dimensions. *SIAM J. Sci. Comput.*, 40(3):A1225–A1249, 2018.
- [2] W.L. Barnes, A. Dereux, and T.W. Ebbesen. Surface plasmon subwavelength optics. *Nature*, 424:824–830, 2003.
- [3] E. Bonnetier and H. Zhang. Characterization of the essential spectrum of the Neumann–Poincaré operator in 2D domains with corner via Weyl sequences. *Rev. Mat. Iberoam.*, accepted 2018.
- [4] D. Colton and R. Kress. *Inverse acoustic and electromagnetic scattering theory*, volume 93 of *Applied Mathematical Sciences*. Springer-Verlag, Berlin, second edition, 1998.
- [5] A.-S. Bonnet-Ben Dhia, C. Carvalho, L. Chesnel, and P. Ciarlet. On the use of perfectly matched layers at corners for scattering problems with sign-changing coefficients. *J. Comput. Phys.*, 322:224–247, 2016.
- [6] Z. Ding. A proof of the trace theorem of Sobolev spaces on Lipschitz domains. *Proc. Amer. Math. Soc.*, 124(2):591–600, 1996.
- [7] L. Greengard and J.-Y. Lee. Stable and accurate integral equation methods for scattering problems with multiple material interfaces in two dimensions. *J. Comput. Phys.*, 231(6):2389–2395, 2012.
- [8] S. Hao, A.H. Barnett, P.G. Martinsson, and P. Young. High-order accurate methods for Nyström discretization of integral equations on smooth curves in the plane. *Adv. Comput. Math.*, 40(1):245–272, 2014.
- [9] J. Helsing. Integral equation methods for elliptic problems with boundary conditions of mixed type. *J. Comput. Phys.*, 228(23):8892–8907, 2009.
- [10] J. Helsing. The effective conductivity of arrays of squares: Large random unit cells and extreme contrast ratios. *J. Comput. Phys.*, 230(20):7533–7547, 2011.
- [11] J. Helsing. Solving integral equations on piecewise smooth boundaries using the RCIP method: a tutorial. *arXiv:1207.6737 [physics.comp-ph]*, revised 2017.
- [12] J. Helsing and A. Holst. Variants of an explicit kernel-split panel-based Nyström discretization scheme for Helmholtz boundary value problems. *Adv. Comput. Math.*, 41(3):691–708, 2015.
- [13] J. Helsing and A. Karlsson. Determination of normalized electric eigenfields in microwave cavities with sharp edges. *J. Comput. Phys.*, 304:465–486, 2016.

- [14] J. Helsing and A. Karlsson. Resonances in axially symmetric dielectric objects. *IEEE Trans. Microw. Theory Tech.*, 65:2214–2227, 2017.
- [15] J. Helsing and K.-M. Perfekt. On the polarizability and capacitance of the cube. *Appl. Comput. Harmon. Anal.*, 34(3):445–468, 2013.
- [16] J. Helsing and K.-M. Perfekt. The spectra of harmonic layer potential operators on domains with rotationally symmetric conical points. *J. Math. Pures Appl.*, in press 2018.
- [17] <http://functions.wolfram.com/03.03.06.0005.01>.
- [18] <http://www.maths.lth.se/na/staff/helsing/animations.html>.
- [19] J.D. Jackson. *Classical Electrodynamics*. John Wiley & Sons:, New York, third edition, 1999.
- [20] R.E. Kleinman and P.A. Martin. On single integral equations for the transmission problem of acoustics. *SIAM J. Appl. Math.*, 48(2):307–325, 1988.
- [21] A. Klöckner, A. Barnett, L. Greengard, and M. O’Neil. Quadrature by expansion: a new method for the evaluation of layer potentials. *J. Comput. Phys.*, 252:332–349, 2013.
- [22] R. Kress and G.F. Roach. Transmission problems for the Helmholtz equation. *J. Math. Phys.*, 19(6):1433–1437, 1978.
- [23] G. Kristensson. *Scattering of electromagnetic waves by obstacles*. Mario Boella Series on Electromagnetism in Information and Communication. SciTech Publishing, an imprint of the IET, Edison, NJ, 2016.
- [24] K.-M. Perfekt and M. Putinar. The essential spectrum of the Neumann–Poincaré operator on a domain with corners. *Arch. Ration. Mech. Anal.*, 223(2):1019–1033, 2017.
- [25] H. Raether. *Surface plasmons on smooth and rough surfaces and on gratings*, volume 111 of *Springer tracts in modern physics*. Springer, 1988.
- [26] V. Rokhlin. Solution of acoustic scattering problems by means of second kind integral equations. *Wave Motion*, 5(3):257–272, 1983.
- [27] F. Wang and Y.R. Shen. General properties of local plasmons in metal nanostructures. *Phys. Rev. Lett.*, 97:206806, 2006.